The Journal of Chemical Physics

Oscillatory instabilities during formic acid oxidation on Pt(100), Pt(110) and Pt(111) under potentiostatic control. II. Model calculations

Cite as: J. Chem. Phys. **107**, 991 (1997); https://doi.org/10.1063/1.474451
Submitted: 16 December 1996 . Accepted: 08 April 1997 . Published Online: 04 June 1998

P. Strasser, M. Eiswirth, and G. Ertl

View Online Export Citation

ARTICLES YOU MAY BE INTERESTED IN

Oscillatory instabilities during formic acid oxidation on Pt(100), Pt(110) and Pt(111) under potentiostatic control. I. Experimental
The Journal of Chemical Physics **107**, 979 (1997); https://doi.org/10.1063/1.474450

Modification of the surface electronic and chemical properties of Pt(111) by subsurface 3d transition metals
The Journal of Chemical Physics **120**, 10240 (2004); https://doi.org/10.1063/1.1737365

Oscillatory CO oxidation on Pt(110): Modeling of temporal self-organization
The Journal of Chemical Physics **96**, 9161 (1992); https://doi.org/10.1063/1.462226

Challenge us.
What are your needs for periodic signal detection?
Watch
Zurich Instruments

AIP Publishing

© 1997 American Institute of Physics.

Oscillatory instabilities during formic acid oxidation on Pt(100), Pt(110) and Pt(111) under potentiostatic control. II. Model calculations

P. Strasser,[a] M. Eiswirth, and G. Ertl
Fritz-Haber-Institut der Max-Planck-Gesellschaft, Faradayweg 4-6, D-14195 Berlin, Germany

(Received 16 December 1996; accepted 8 April 1997)

A kinetic model is developed for the electrocatalytic oxidation of formic acid on Pt under potentiostatic control. The model development proceeds stepwise via a simple model of the electrocatalytic CO oxidation. The full model consists of four coupled, nonlinear ordinary differential equations. The scanned and stationary current/outer potential (I/U) behavior, stationary current oscillations, two-parameter bifurcation diagrams and stirring effects are simulated using realistic model parameters. The numerical findings are found to be consistent with the experimental results given by Strasser *et al.* The model reproduces period-1 as well as mixed-mode oscillations. Furthermore, a mechanistic analysis of the model was performed: two suboscillators are identified whose characteristics allow a plausible interpretation of the observed dynamics. After a classification of the suboscillators into previously described categories, an attempt is made to identify the minimal mechanistic requirements for electrochemical current oscillations. © *1997 American Institute of Physics.* [S0021-9606(97)01327-5]

I. INTRODUCTION

In a previous paper,[1] an experimental investigation of the electrocatalytic formic acid oxidation reaction on Pt(100), Pt(110) and Pt(111) under potentiostatic control was reported. Current oscillations were observed on all three single crystals. As source of the instability, we proposed the crucial role of the interplay of both electrical quantities, i.e., the double layer potential ϕ and the current density I, and chemical quantities such as the concentrations of the electroactive species. We also gave a descriptive interpretation of how we consider the sustained current oscillations to arise. Here we present a detailed numerical study of a kinetic model in order to test our mechanistic hypotheses.

There are several kinetic models of electrocatalytic oscillators in the literature which differ significantly in their ability to reproduce experimental findings under realistic conditions.[2–14] A first attempt to come up with a kinetic model for the galvanostatic formic acid oxidation on Pt was undertaken by Albahadily and Schell who employed a six- and seven-variable model. As the source of the instability, they proposed a kinetic rate law of the removal reaction of a poisoning intermediate (CO) which was set to be autocatalytic with respect to the vacant surface sites (vacant site requirement). In a more recent study Okamoto *et al.*[14] investigated a three-variable model and reported potential oscillations that were similar in shape to those obtained in experiments.

In the present paper, we will test our hypotheses made in Ref. 1. To this end, we stepwise develop a realistic kinetic model for the FA oxidation (Section IV) starting out with the CO oxidation (Section II and III) as was done in the previous experimental study. A detailed numerical analysis of the model employing conditions close to experiments is given in Section V. Finally, the mechanistic reasons for the occurrence of instabilities, simple oscillations and mixed-mode oscillations are discussed in Section VI.

II. A MODEL FOR THE ELECTROCHEMICAL CO OXIDATION

Based on recent results,[15–17] there now exists agreement on the crucial involvement of CO as a poisoning intermediate in the indirect oxidation path of the electrochemical formic acid (FA) oxidation: Under conditions where oscillations occur during FA oxidation, the poisoning of the catalytic surface by CO adsorption leads to an increase of the double layer potential ϕ, which in turn results in the formation of surface hydroxides such as Pt–OH; these species then remove the adsorbed CO by oxidation to CO_2. The CO oxidation therefore constitutes a submechanism of the full FA mechanism. So, it is obvious that an experimental and numerical investigation of CO oxidation is useful to gain insight into the indirect oxidation path of the FA mechanism. Moreover, once a kinetic model of the CO reaction has been constructed, it can be used as a submodel of a model of FA oxidation.

A. Chemical model

In view of the experimental conditions under which our current/outer potential (I/U) measurements were obtained, we assume CO to be reversibly transported by diffusion between the bulk solution and the double layer resulting in a time-dependent concentration profile across the diffusion layer. Denoting the CO concentration in the bulk by CO_{bulk} and the concentration of CO just outside the double layer as CO_{dl} we write the diffusive transport of CO as

$$CO_{bulk} \overset{D}{\rightleftharpoons} CO_{dl}. \tag{1}$$

The superscript D suggests the dependence of the rate of this pseudoreaction on the diffusion constant of CO, D_{CO}. Ad-

[a]Electronic mail:peter@pippi.rz-berlin.mpg.de

sorption and desorption of CO on the catalytic surface is taken care of by the potential independent scheme

$$CO_{dl} + * \rightleftharpoons CO_{ad}, \tag{2}$$

where * symbolizes a vacant surface site. The subscript ad indicates species adsorbed on the surface. It is assumed that CO is bound linearly to the surface needing one adsorption site.

At higher double layer potentials ϕ, a reversible oxidation of water molecules to surface hydroxides (OH) sets in followed by the irreversible formation of higher valent Pt oxides such as Pt–O. For simplicity and transparency of the numerical model, however, we consider OH to be the dominant oxygen species involved in the mechanism and do not include any of the further oxygen species. Our assumption is experimentally justified by our attempt to keep the applied potential well below the region where irreversible formation of oxygen species was observed. Thus, our chemical equation reads

$$H_2O + * \rightleftharpoons OH_{ad} + H^+ + e^-. \tag{3}$$

The formation of electrons causes the reaction constants of this reaction to depend explicitly on the double layer potential ϕ.

Finally, CO_{ad} and OH_{ad} are assumed to react in a potential dependent reaction forming the final product CO_2:

$$CO_{ad} + OH_{ad} \rightarrow CO_2 + 2* + e^- + H^+. \tag{4}$$

Note that reaction (4) is not assumed to involve an additional free surface site.

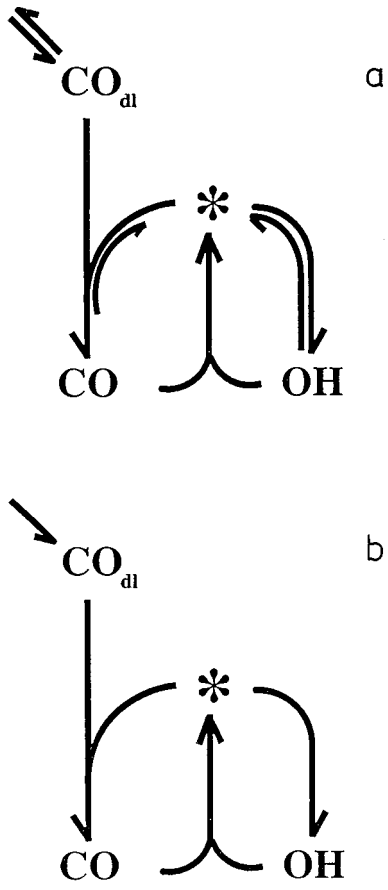

FIG. 1. (a) Network diagram of the CO oxidation mechanism. CO_{dl}, *, CO and OH denote CO at the double layer, the vacant surface sites, adsorbed CO and adsorbed OH, respectively. The arrows indicate the chemical (pseudo)reactions. The total number of barbs and arrows encode the stoichiometric coefficient of the respective species. (b) Current diagram of unstable steady state subnetwork which is contained in the CO model. This unstable network leads to bistability in some region of parameter space. Since no electrical quantity is involved the instability is purely chemical and thus numerically observable under truly potentiostatic conditions, i.e., for constant ϕ.

B. Mathematical model

For the purpose of a numerical analysis, the chemical model given above is to be translated into a mathematical model describing the time evolution of the concentrations of species essential for the mechanism. The chemical model suggests that the concentrations of CO in solution, of CO_{ad} and OH_{ad} have to be included as dynamical variables. The exact solution of the problem involves the solution of a partial differential equation (PDE) for the concentration gradient of CO across the diffusion layer. Following Koper and Wolf,[11,18] however, we avoid solving a PDE for each time step. Instead, we truncate this problem by only considering the concentration of CO at the boundary between diffusion layer and double layer, in the chemical model denoted as CO_{dl}, as dynamical variable and by assuming a linear concentration gradient across a diffusion layer of fixed thickness δ at all times. These assumptions imply an immediate relaxation to a linear concentration profile, i.e., the steady-state profile, for nonzero net fluxes through the diffusion layer. We are aware of the fact that under experimental conditions the thickness δ certainly is subject to periodic variations as the current I oscillates. Following Ref. 18 we therefore consider δ to be an average thickness during oscillations. To complete the kinetic equation of the variable CO_{dl} one has to add its removal due to CO adsorption according to Eq. (2). Note that throughout this paper surface concentrations of adsorbed species such as CO_{ad} and OH_{ad} are normalized with respect to the total concentration of surface sites, S_{tot}, providing the dimensionless surface coverage θ_i of a species i as the actual dynamical variable. The measured I/U curves of the CO oxidation given in Ref. 1 (Fig. 1 on Pt single crystals and Fig. 2 on polycrystalline Pt) indicate an asymmetric inhibition of CO_{ad} and OH_{ad}, i.e., the fact that a high CO coverage blocks the adsorption of OH completely [see the CV of Pt(100)], however, that at a high coverage of OH at higher potentials U there is still a finite CO oxidation current discernible on top of the current caused by OH adsorption; obviously, the OH coverage does not completely block all sites allowing for sustained CO adsorption and oxidation. The asymmetric inhibition is included in our model by means of an empirical factor f which modifies the hindrance factor yielding $(1-\theta_{CO}-f\theta_{OH})$. A value of f smaller than 1 leads to finite CO adsorption rate sites even if $\theta_{OH}=1$, i.e., has reached its saturation value.

The final equation for CO_{dl} then reads

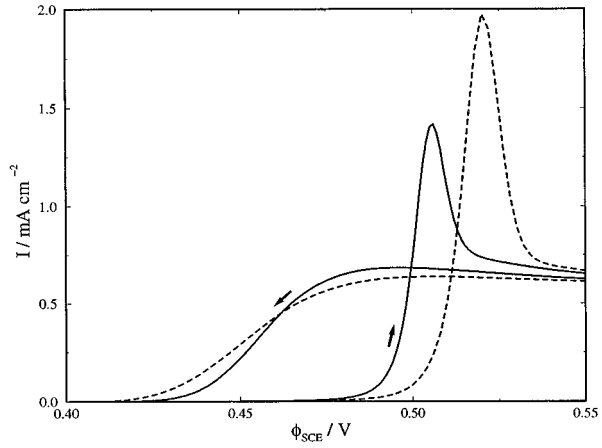

FIG. 2. Calculated CV for the CO oxidation using model Eqs. (5)–(7). The double layer potential was cycled between 0 and 1.0 V. Model parameters (see also Tables I and II) : pH=3, $f=0.99$, solid curve: potential scan rate 10 mV/s, dashed curve: 20 mV/s. The arrows indicate the anodic and cathodic scan. For a comparison with experiments see Fig. 2 in Ref. 1.

$$\frac{d\mathrm{CO}_{dl}}{dt}=\frac{2D_{\mathrm{CO}}}{\delta^2}(\mathrm{CO}_{bulk}-\mathrm{CO}_{dl})-\frac{2000S_{tot}}{\delta}k_{ads,\mathrm{CO}}\times(1-\theta_{\mathrm{CO}}-f\theta_{\mathrm{OH}})\mathrm{CO}_{dl}-k_{des,\mathrm{CO}}\theta_{\mathrm{CO}}. \tag{5}$$

The factor 1000 comes in because S_{tot} and CO_{dl} are given in mol/cm^2 and mol/l, respectively.

For the charge transfer controlled reactions Eqs. (3) and (4), we use Butler–Volmer type charge transfer kinetics.[19] Since the exact equilibrium potential ϕ_{eq} of these reactions is not known, we include the exponential term into the rate constants thereby reducing the number of adjustable parameters. Denoting the symmetry factors of reactions (3) and (4) and the double layer potential as α_1, α_2 and ϕ, respectively, and using the conventional letters for the Faraday constant (F), the gas constant (R) and the absolute temperature (T), we write for the evolution of the OH coverage

$$\frac{d\theta_{\mathrm{OH}}}{dt}=k_{ads,\mathrm{OH}}(1-\theta_{\mathrm{OH}}-\theta_{\mathrm{CO}})e^{\alpha_1(F/RT)\phi}-k_rS_{tot}\theta_{\mathrm{CO}}\theta_{\mathrm{OH}}e^{\alpha_2(F/RT)\phi}-k_{des;\mathrm{OH}}\theta_{\mathrm{OH}}e^{-(1-\alpha_1)(F/RT)\phi}. \tag{6}$$

$k_{ads,\mathrm{OH}}$, $k_{des,\mathrm{OH}}$ and k_r are the rate constants of OH adsorption, OH desorption and of reaction between OH_{ad} and CO_{ad}. It should further be noted that due to the formation of protons the equilibrium potentials ϕ_{eq} of reactions (3) and (4) are dependent on the pH of the electrolyte. Since ϕ_{eq}, however, is included into the rate constants, it follows that we get a pH dependence of the rate constants $k_{ads,\mathrm{OH}}$,$k_{des,\mathrm{OH}}$ and k_r. This is illustrated by the following relation, where k',β, g and k denote constants and kg^{pH} symbolizes the final pH dependent rate constant:

$$k'e^{\beta[\phi-(\phi_{eq}-0.059\mathrm{pH}]}=k'e^{-\beta\phi_{eq}}e^{\beta 0.059\mathrm{pH}}e^{\beta\phi}=kg^{\mathrm{pH}}e^{\beta\phi}.$$

Finally, we formulate the kinetic equation of θ_{CO}:

$$\frac{d\theta_{\mathrm{CO}}}{dt}=k_{ads,\mathrm{CO}}\mathrm{CO}_{dl}(1-\theta_{\mathrm{CO}}-f\theta_{\mathrm{OH}})-k_rS_{tot}\theta_{\mathrm{CO}}\theta_{\mathrm{OH}}e^{\alpha_2(F/RT)\phi}-k_{des,\mathrm{CO}}\theta_{\mathrm{CO}}. \tag{7}$$

All experimental results on CO oxidation given in Ref. 1 were obtained in solutions of high ionic conductivities which justifies neglecting the ohmic potential drop across the portion of the electrolyte between reference and working electrode. The double layer potential ϕ therefore was equal to the applied constant outer potential U during the measurements (truly potentiostatic conditions) and we did not include the double layer potential ϕ as an additional dynamical variable.

III. ANALYSIS OF THE CO OXIDATION MODEL

A. Qualitative network analysis

Figure 1(a) displays the stoichiometric network diagram of the CO oxidation model given by Eqs. (5)–(7). The arrows connecting the chemical species symbolize the chemical (pseudo)reactions of the model mechanism. The number of feathers and barbs correspond to the stoichiometric coefficients as given in the chemical formulation Eqs. (1)–(4). If the stoichiometric coefficient of a species which is consumed during a reaction equals 1, no feather is drawn at the corresponding reaction arrow.[20]

It has been shown[20,21] that the stoichiometric and kinetic coefficients of a chemical reaction mechanism can be used for a rapid assessment of the mechanism's ability to exhibit a dynamical instability due to an autocatalysis at some point in parameter space. The method to achieve this is called stoichiometric network analysis (SNA).

Applying SNA to our simple network diagram, it turns out that there is an unstable subnetwork contained in the full model. This unstable submechanism is shown in Fig. 1(b). According to Ref. 21, the free surface sites as well as adsorbed OH form an autocatalytic cycle which is destabilized by the CO_{dl} species. In appropriate combination with the remaining stabilizing reactions of the complete model, this unstable core of the chemical network can give rise to a bistability between a predominantly CO and OH covered surface, as was confirmed numerically. Note that the instability stems from the chemical network only and does not involve any electrical variables. In experimental terms, the presence of CO_{dl} as a dynamical variable would require the absence of strong stirring which would constrain the value of CO_{dl} to the value of CO_{bulk}. In fact, the bistability is observable in numerical simulations only for large values of the diffusion layer thickness δ.

B. Numerical simulations

Table I shows the values of the numerical parameters D_{CO} and CO_{bulk}. The thickness of the diffusion layer δ of $4\cdot10^{-4}$ cm corresponds to a very high rotational frequency of $28\cdot10^3$ rpm.

TABLE I. Parameters used in simulations of the CO oxidation model Eqs. (5)–(7) under potentiostatic control. Other parameters are given in the figure captions of the respective calculations.

Parameter	Value	Unit
D_{CO}	5×10^{-5}	cm^2/s
CO_{bulk}	10^{-3}	mol/ℓ
δ	4×10^{-4}	cm
S_{tot}	3×10^{-9}	mol/cm^2
T	298	K

The other parameters were adjusted in the course of the numerical simulations. The pH dependence stems from the fact that protons are produced during reactions (3) and (4). The parameter values were used for our simulations of I/U curves of the CO oxidation discussed in this section. In order to match experimental conditions the pH was set to 3.

To integrate the coupled set of nonlinear ordinary differential equations (ODEs) we used a solver for stiff problems taken from the lsode-package.[22] The implemented algorithm is a higher-order Adams–Molton-type predictor-corrector method. The integration was started at a low value of the potential ϕ ($\phi\approx0$ V). All simulations refer potentials with respect to the standard calomel electrode (SCE). During integration the potential ϕ was periodically cycled between 0 and 1 V. Figure 2 displays the numerical results at a potential sweep rate of 10 and 20 mV/s. The numerical I/U curve obtained is in good qualitative and quantitative agreement with the experimentally measured curve on polycrystalline Pt (Ref. 1, Fig. 2). First of all, one recognizes the familiar shape of experimental I/U curves characterized by a potential dependent blocking of CO and OH at low and high potentials ϕ, respectively. At a sweep rate of 20 mV/s, the CO coverage remains high up to $\phi\approx0.5$ V preventing OH from adsorption. At $\phi\approx0.53$ V, a sudden ignition process starts during which OH adsorbs and removes all CO by reaction (4). At higher double layer potentials, the current density I remains finite at around $0.6mA/cm^2$. On the reverse scan, the current density remains roughly unchanged even beyond the ''ignition potential.'' OH starts to desorb allowing for CO to readsorb. Similar to experiments, as the sweep rate is decreased, the current I on the reverse scan shows a hump right before falling off to small values.

IV. A MODEL FOR THE ELECTROCHEMICAL FORMIC ACID OXIDATION

A. Chemical model

In this section we will extend the model for the CO oxidation further so as to achieve a description of the dynamics of the FA oxidation reaction. Instead of using the volume species CO_{dl} we now introduce the corresponding formic acid species FA_{dl}. As described in Section II, this amounts to a simplified modeling of the diffusional mass transport assuming a diffusion layer of fixed thickness δ and a linear concentration gradient of FA across the diffusion layer at all times.

The poisoning of the surface at low potentials ϕ is again considered to be due to CO adsorption only; however, the intermediate poison CO_{ad} is now assumed to be formed by an irreversible, potential-independent decomposition of formic acid just outside the double layer:

$$FA_{dl}+*\rightarrow CO_{ad}+H_2O.$$

k_{poison} denotes the chemical rate constant. To avoid the unphysical situation of a surface completely blocked by CO, we also include the desorption of CO_{ad} even though from gas phase studies on Pt the rate constant of the desorption is known to be extremely small.

At higher potentials, CO_{ad} is removed by OH_{ad} as in Eq. (4) of the CO oxidation model. The poisoning by and the removal of CO_{ad} constitute the indirect path of the FA oxidation model.

In addition, we have to take the direct oxidation path of FA into consideration which occurs via at least one highly reactive intermediate. For the overall reaction scheme we write[7,12]

$$FA_{dl}+*\rightarrow CO_2+*+2H^++2e^-.$$

This overall reaction is further chemically resolved as follows: We assume the initial adsorption of formic acid on free surface sites yielding the adsorbed species FA_{ad} followed by the reaction path given in Ref. 12. The chemical equations read

$$FA_{dl}+*\rightleftharpoons FA_{ad}, \tag{8}$$

$$FA_{ad}\rightarrow \cdot COOH_{ad}+H^++e^-, \tag{9}$$

$$\cdot COOH_{ad}\rightarrow CO_2+H^++e^-+*. \tag{10}$$

This detailed formulation follows partly the suggestions of previous studies.[7,12,23] Due to insufficient experimental information as to the detailed kinetics of the dehydrogenation reactions (9) and (10), any possible vacant site requirement is neglected. The third reaction step can safely be assumed to be very fast compared to the first and second which allows adiabatic elimination of the radical species $\cdot COOH_{ad}$. Consequently, depending on the concentration of FA_{dl} and of the free surface sites, the rate determining step is either the first or the second reaction thereby taking care of both charge-transfer controlled and adsorption controlled reaction conditions. When formulating this reaction sequence in mathematical terms, we will make an additional adiabatic elimination of FA_{ad} leaving FA_{dl} as the only dynamical formic acid species in the model.

In contrast to Ref. 12, we do not explicitly consider the time evolution of protons and hydroxide ions. Instead, we assume the dissociation of water at equilibrium at all times. Moreover, the diffusion of protons into the bulk solution is assumed to be so fast as to obtain a constant pH across the double layer. The complete chemical model for the FA oxidation reaction finally reads

$$FA_{bulk}\rightleftharpoons FA_{dl}, \tag{11}$$

$$FA_{dl}+*\rightarrow CO_2+*+2H^++2e^-, \tag{12}$$

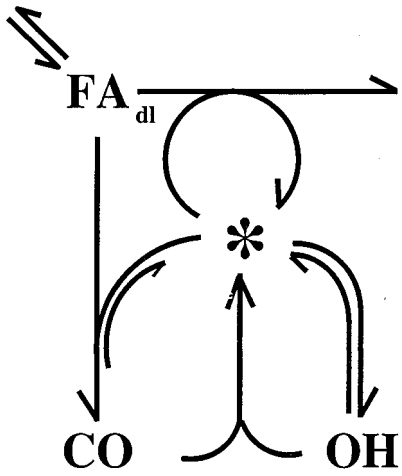

FIG. 3. Network diagram of the FA oxidation mechanism. The species and (pseudo)reaction arrows are analogous to Fig. 1(a).

$$\mathrm{FA}_{dl}+*\rightarrow \mathrm{CO}_{ad}+\mathrm{H_2O}, \tag{13}$$

$$\mathrm{CO}_{ad}\rightarrow \mathrm{CO}_{f}+*, \tag{14}$$

$$\mathrm{H_2O}+*\rightleftharpoons \mathrm{OH}_{ad}+\mathrm{H}^{+}+e^{-}, \tag{15}$$

$$\mathrm{CO}_{ad}+\mathrm{OH}_{ad}\rightarrow \mathrm{CO_2}+2*+e^{-}+\mathrm{H}^{+}, \tag{16}$$

with reaction step (12) being the sum of reactions (8)–(10). Again, reaction (16) does not consider any vacant site requirement as proposed by Wojtowicz *et al.*[24] and as implemented later in a galvanostatic 6-variable FA model of Ref. 7 because there is no experimental evidence that the reaction of CO with OH requires additional unoccupied sites. According to the assumptions made above concerning oxygen species at higher potentials this model only provides an adequate description at low double layer potentials where oscillatory instabilities are observed.[1] Figure 3 depicts our chemical network in a more illustrative way: chemical reactions are drawn as arrows connecting the dynamical variables. The kinetics and stoichiometry of the reactions are encoded in the number of feathers and barbs as described in Section II. One recognizes the central role of the free surface sites. Furthermore, the CO oxidation submechanism is well discernible in the lower portion of the network diagram.

B. Mathematical model

The dynamical variables are the formic acid concentration at the double layer, FA_{dl}, the coverage of CO, θ_{CO}, and the coverage of OH, θ_{OH}. In contrast to the CO model, however, we now aim at a simulation of potentiostatic I/U characteristics at high ohmic resistances R as well. In Ref. 1 it is shown that especially for high values of R complex instabilities can be observed during formic acid oxidation. As outlined in Ref. 1 high values of R cause an additional IR drop and allow for the double layer potential ϕ to vary at constant outer potential U. The double layer potential ϕ therefore has to be included in the model as an additional dynamical variable.

The equation for FA_{dl} was set up in analogy to Eq. (5). Two reaction rate terms, v_{direct} and v_{poison}, resulting from processes of Eq. (12) and Eq. (13) contribute to the consumption of FA_{dl}. The model equation reads

$$\dot{\mathrm{FA}}_{dl}=\frac{2D_{\mathrm{FA}}}{\delta^2}(\mathrm{FA}_{bulk}-\mathrm{FA}_{dl})-\frac{2000S_{tot}}{\delta}(v_{direct}+v_{poison}). \tag{17}$$

Here, D_{FA} and FA_{bulk} denote the diffusion coefficient and the bulk concentration of formic acid, respectively.

The velocity for the direct oxidation path, v_{direct}, becomes after adiabatic elimination of FA_{ad}

$$v_{direct}=\frac{k_d e^{(\alpha_3 F/RT)\phi}k_{ads;\mathrm{FA}}\mathrm{FA}_{dl}}{k_d e^{(\alpha_3 F/RT)\phi}+k_{ads;\mathrm{FA}}\mathrm{FA}_{dl}}(1-\theta_{\mathrm{CO}}-f\theta_{\mathrm{OH}}). \tag{18}$$

The parameters k_d, α_3 and $k_{ads;\mathrm{FA}}$ represent the rate constant and the symmetry factor of reaction (9) and the adsorption constant of FA_{dl}, respectively. Note that we have neglected the expression of desorption of FA_{ad} in the expression for v_{direct}. Similar to the CO model, the empirical factor f is to take care of the observed incomplete blockage of the FA oxidation reaction by adsorbed OH.

The expression for v_{poison} is straightforward:

$$v_{poison}=k_{poison}\mathrm{FA}_{dl}(1-\theta_{\mathrm{CO}}-\theta_{\mathrm{OH}}). \tag{19}$$

The factor f is only included in the rate law of the direct FA oxidation Eq. (18) since it is assumed that the observed finite oxidation current at high OH coverage is due to sustained dehydrogenation of FA.

The kinetic equations for the surface coverage of CO and OH are adopted from our CO model. The only modification is the use of expression (19) for the CO production instead of CO adsorption. The final equations are

$$\dot{\theta}\theta_{\mathrm{OH}}=k_{ads;\mathrm{OH}}(1-\theta_{\mathrm{CO}}-\theta_{\mathrm{OH}})e^{\alpha_1(F/RT)\phi}-k_r S_{tot}\theta_{\mathrm{CO}}\theta_{\mathrm{OH}}e^{\alpha_2(F/RT)\phi}-k_{des;\mathrm{OH}}\theta_{\mathrm{OH}}e^{-(1-\alpha_1)(F/RT)\phi}, \tag{20}$$

$$\dot{\theta}_{\mathrm{CO}}=v_{poison}-k_r S_{tot}\theta_{\mathrm{CO}}\theta_{\mathrm{OH}}e^{\alpha_2(F/RT)\phi}-k_{des;\mathrm{CO}}\theta_{\mathrm{CO}}. \tag{21}$$

Although it has been shown in Ref. 12 that purely chemical oscillatory instabilities, i.e., oscillations under strictly potentiostatic conditions, are possible in the dual channel FA oxidation mechanism, if the pH is taken into account, the experimental results in Ref. 1 strongly suggest that the pH is nonessential and purely chemical instabilities did not occur for the conditions used. Consequently, the modeling has to explicitly consider the time variations of the double layer potential ϕ (also denoted as ϕ_{dl} in the figures) which requires the introduction of an additional equation. Considering capacitive and faradaic currents and using the equation of charge conservation,[4,7,11,25] we formulate the kinetic equation for ϕ as

$$\dot{\phi}=\frac{1}{C_{dl}}(j_{tot}-j_{direct}-j_{ads;\mathrm{OH}}-j_r+j_{des;\mathrm{OH}}), \tag{22}$$

TABLE II. Parameters used in simulations of the CO oxidation. The same values (except $k_{ads;CO}$ and f) were also used in simulation of the FA oxidation model.

Parameter	Value	Unit
α_1	0.4	-
α_2	0.5	-
$k_{ads,OH}$	$7.72\times10^{-3}\cdot2.5^{pH}$	s^{-1}
$k_{des,OH}$	$3.0\times10^{6}\cdot0.25^{pH}$	s^{-1}
$k_{ads,CO}$	1.0×10^{5}	ℓ/mol s
$k_{des,CO}$	1.33×10^{-3}	s^{-1}
k_r	$5.06\times10^{3}\cdot3.1^{pH}$	cm^2/mol s
f	0.99	-

where C_{dl} denotes the differential double layer capacity; the j_i represents the respective faradaic current densities of the electrochemical reactions (12), (15) and (16), whereas j_{tot} is the total current density flowing through the cell. Note that reduction currents and oxidations currents are written with a negative and positive sign, respectively.

The general expression for the j_i is given by

$$j_i = nFS_{tot}v_i, \tag{23}$$

with n and v_i denoting the number of electrons exchanged in the reaction and the reaction rate, respectively.

Finally, in order to model potentiostatic conditions, an expression for j_{tot} in dependence of the constant outer potential U is required:

$$j_{tot} = \frac{U-\phi}{AR}. \tag{24}$$

R denotes the ohmic resistance caused by low ionic concentrations or by an outer ohmic resistor in series with the electrochemical cell; A stands for the area of the electrode.

V. ANALYSIS OF THE FORMIC ACID OXIDATION MODEL

Tables II and III show the model parameters used during the numerical analysis of the FA model. The unknown kinetic constants $\alpha_3, f, k_d, k_{poison}$ and $k_{ads;FA}$ were adjusted and optimized in the simulations. The remaining parameters (pH and scan rate) are given when discussing the simulations. All bifurcation diagrams were computed using the AUTO program.[26]

TABLE III. Parameters used in simulations of the FA oxidation model. All remaining parameters are given in Table II or in the figure captions of the respective calculations. The value of δ depends on stirring. k_{poison} was chosen differently in order to model the different surface orientations.

Parameter	Value	Unit
D_{FA}	2.5×10^{-5}	cm^2/s
C_{dl}	20×10^{-6}	F/cm^2
A	0.625	cm^2
δ	$2\times10^{-4}/3\times10^{-2}$	cm
FA_{bulk}	0.05	mol/ℓ
α_3	0.5	-
k_{poison}	6–60	ℓ/mol s
$k_{ads,FA}$	1.3×10^{3}	ℓ/mol s
k_d	$9.03\times10^{-4}\cdot3.1^{pH}$	s^{-1}
f	0.995	-

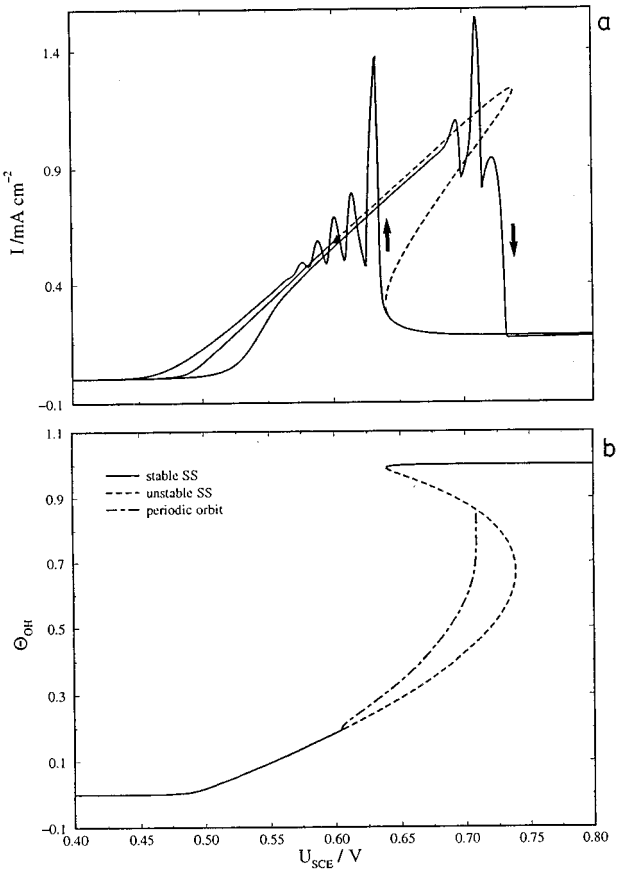

FIG. 4. (a) Calculated CV and stationary I/U curve for the FA oxidation model [Eqs. (17)–(24)]. The anodic and cathodic scans are indicated by arrows. Sharp current spikes are seen during both scan directions. Furthermore, a hysteresis between a low-current steady state and an oscillatory high-current state is observed. Model parameters (see also Tables II and III): $T=298$ K, pH=1, $\delta=3\times10^{-2}$, $R=300\ \Omega$, $k_{poison}=60$ ℓ/mol s, scan rate 10 mV/s. The stationary curve corresponds to an infinitely slow scan rate. The transition between stable current behavior and oscillatory current behavior was found to be a Hopf bifurcation point (solid triangle, $U=0.6$ V) at low values of U. The stationary curve further shows the experimentally unaccessible unstable steady state branch (dashed line) which undergoes two saddle node bifurcation ($U=0.74$ V, $U=0.64$ V) before regaining stability on the low-current branch. b) Calculated one-parameter bifurcation diagram of the FA model for model parameters as given in (a). The steady state coverage of OH, θ_{OH} is plotted against the applied potential U. The solid dashed lines indicate stability and instability, respectively. The dotted-dashed line shows the amplitude of the stable periodic orbits born in the Hopf bifurcation. At the value of U where the dotted-dashed line disappears the limit cycle collides with the saddle in a saddle-loop bifurcation. Beyond this potential value there is no stable state other than the low-current, OH-covered steady state.

A. Oscillatory instabilities in scanned and stationary *I/U* curves

In Fig. 4(a), a scanned (arrows indicate the scan direction) as well as a stationary I/U curve are shown for $R=300\ \Omega, k_{poison}=60$, pH=1 and a scan rate of $\nu=10$ mV/s. The thickness of the diffusion layer δ was cho-

sen to be large ($3 \cdot 10^{-2}$) corresponding to unstirred conditions. The outer potential U was cycled between 0 and 1 V.

From Fig. 4(a) it can be seen that as U increases, the current I slowly increases beyond $U \approx 0.5$ V which corresponds to the ''ignition'' potential of OH adsorption in our CO simulations. At higher values of U, the current starts exhibiting sharp spikes until it rapidly falls off to a low, but still finite value of I. This deactivated state is characterized by a $\theta_{OH} \approx 1$. On the reverse scan, the current remains low down to $U \approx 0.63$ V, then shoots up rapidly performing a periodic spiking. Now, the surface becomes increasingly blocked by adsorbed CO.

The stationary I/U in Fig. 4a is seen to be between the anodic and cathodic scan. It corresponds to a hypothetical cyclic voltammogram (CV) measured with ν going to zero. The line style of the stationary curve encodes the stability of the system. A solid (dashed) line symbolizes stability (instability). The solid triangle shows where the oscillatory instability sets in. On the cathodic scan, the current follows the limit cycle behavior immediately after the system has passed the lower saddle node and has jumped to high currents, whereas on the anodic scan, the limit cycle past the Hopf bifurcation needs more time to dominate the behavior of the scan before the current falls off onto the predominantly OH-covered steady-state branch as the limit cycle disappears ($U \approx 0.73$ V).

More detailed insight into the bifurcation behavior of the limit cycle is provided by the one-dimensional bifurcation diagram shown in Fig. 4(b). The steady state values of θ_{OH} are plotted against U. The amplitude curve (dotted-dashed) is seen to increase with increasing U until it reaches its maximum and coincides with the unstable saddle curve. Beyond that point, the limit cycle disappears. This scenario is reminiscent of the collision of a stable limit cycle with a saddle point resulting in the destruction of the limit cycle in a so-called saddle-loop infinite-period bifurcation. Hence, Fig. 4(b) confirms the conjecture as to the type of bifurcation occurring at the upper boundary of the oscillatory region. A typical time series of the stable limit cycles is shown in Fig. 5.

The simulated CV in Fig. 4(a) as well as the sustained current oscillations are seen to resemble the experimental findings on Pt(100) shown in Fig. 8 of Ref. 1.

Next, we report the model dynamics for a smaller rate constant of the poisoning reaction (13). This is done because the rate of poisoning was found to be a crucial structure-sensitive parameter and was reported to be much smaller on Pt(111) compared to Pt(100).[27] We chose $k_{poison} = 6$ and $R = 700\ \Omega$ leaving all other model parameters as in Fig. 4. The scanned CV as well as the hypothetical stationary I/U behavior are shown in Fig. 6(a). Periodic current variations are only discernible during the anodic scan. Sweeping cathodically, the current density simply jumps discontinuously from the low-current near the high-current steady state without showing any damped periodic behavior. This behavior becomes clear when looking at the stationary I/U curve and its stability: the Hopf bifurcation (0.77 V) is now located to the right of the low-current saddle-node bifurcation (0.71 V).

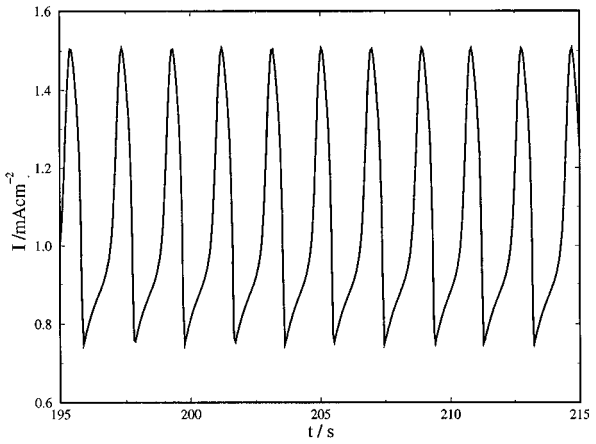

FIG. 5. Calculated time series at constant outer potential $U = 0.7$ V. All other model parameters as given in Fig. 4.

Hence, the regime of stable oscillations is inaccessible on the cathodic potential scan.

The bifurcation diagram shown in Fig. 6(b) reveals a very similar bifurcation sequence as before. The time series at $U = 0.9$ V seen in Fig. 7 shows stable current oscillations which are characterized by a comparatively fast increase of I followed by an initially very slow decrease; the decrease of current is considerably accelerated before the current starts rising again.

A comparison of the numerical CV and of the oscillatory wave form (using a small rate of poisoning) with the experimentally measured CV on Pt(111) (Fig. 10 in Ref. 1) reveals a qualitative agreement.

By looking at the phase relations of the kinetic variables the descriptive interpretations are to be checked that have been put forward to explain oscillatory behavior in the FA system.[7,12,23,28,29] Figures 8(a)–8(c) show the time evolution of $\theta_{CO}, \theta_{OH}, FA_{dl}$ and ϕ for the parameter values used in Fig. 7. The variables θ_{OH} and ϕ are nearly in phase suggesting θ_{OH} to be a fast variable which follows the variations of ϕ almost without delay. The potential independent CO production, in contrast, appears to proceed on a much slower time scale and exhibits a considerable phase shift. The slow increase of θ_{CO} is accompanied by the simultaneous slow increase of the ϕ and θ_{OH}. At a threshold value of ϕ, a very fast adsorption of OH sets in leading to a simultaneous shoot up of the total coverage and ϕ. Being consumed by the reaction which carries the major portion of the overall current density, FA_{dl} is high whenever the total surface coverage is high and, consequently, the value of I is low. FA_{dl} exhibits an anti-phase behavior compared to θ_{CO}: During the slow increase of θ_{CO} FA_{dl} falls off at a similar rate.

B. Bifurcation analysis and oscillatory submechanisms

Complex dynamics of chemical reaction networks is often the result of an interaction of more than one unstable feature within the mechanism. A decomposition of the complex network into simpler networks helps to extract possibly

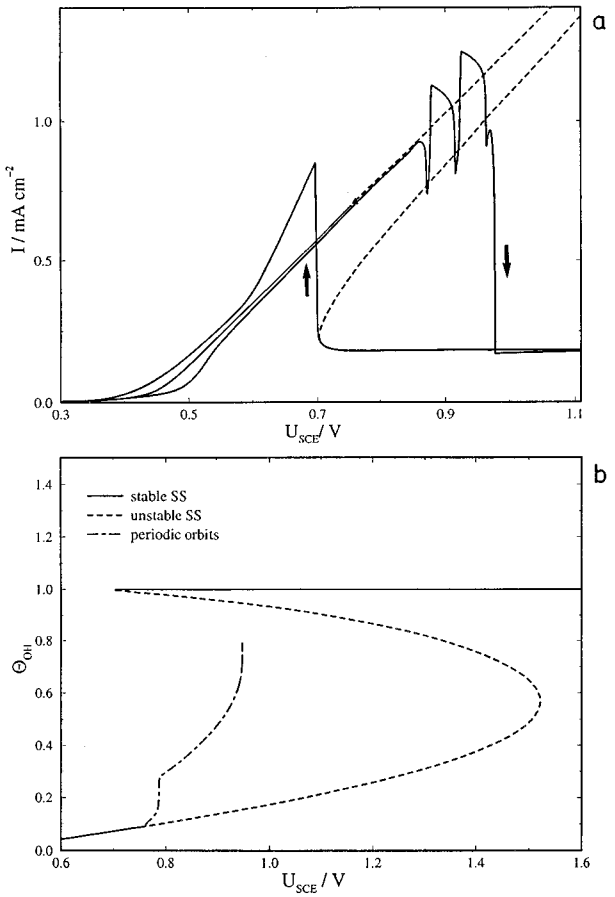

FIG. 6. (a) Calculated CV and stationary I/U curve for the FA oxidation model. The anodic and cathodic scans are indicated by arrows. Broad current spikes are seen on the anodic scan only. A broad hysteresis between a low-current steady state and an oscillatory high-current state is observed. Model parameters (see also Tables II and III): $T=298$ K, pH=1, $\delta=3\times10^{-2}$, $R=700\ \Omega$, $k_{poison}=6$ ℓ/mol s, scan rate 10 mV/s. The solid and dashed stationary curves denote stable and unstable steady states. The solid triangle symbolizes the location of the Hopf bifurcation ($U=0.77$ V). (b) Calculated one-parameter bifurcation diagram of the FA model for model parameters as given in (a). The steady state coverage of OH, θ_{OH} is plotted against the applied potential U. The solid line and dash line indicate stability and unstability, respectively. The dotted-dashed line show the amplitude of the stable periodic orbits born in the Hopf bifurcation. At the value of U where the dotted-dashed line disappears the limit cycle collides with the saddle in a saddle-loop bifurcation. Beyond this potential value there is no stable state other than the low-current, OH-covered steady state.

different sources of instabilities.[21] The knowledge of the dynamics of such subnetworks then can provide an understanding of the observed behavior of the full chemical network.

In this section we show how the complete FA mechanism [Eqs. (17),(20),(21),(22)] can be decomposed into two suboscillators which consist of the same source of instability (autocatalysis) but exhibit different negative feedback loops. Their respective contributions to the observed overall dynamics is described and related to the experimental findings described in Ref. 1.

1. Bifurcation behavior of the full FA mechanism

Figure 9 depicts a two-parameter bifurcation diagram of the full FA model under unstirred conditions ($\delta=3\cdot10^{-2}$)

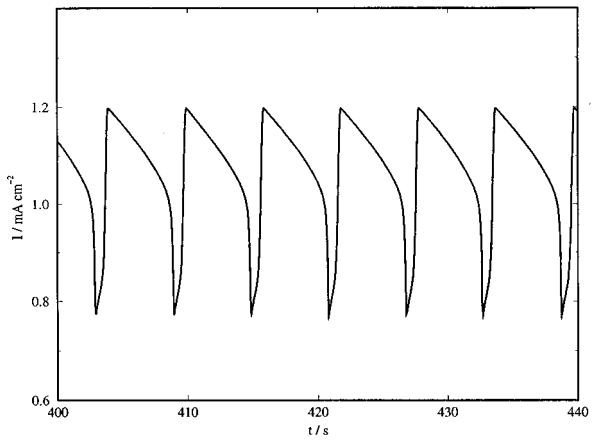

FIG. 7. Calculated time series at constant outer potential $U=0.9$ V. All other model parameters as given in Fig. 6.

in dependence of the parameters U and R. The large value of δ ensures that the variable FA_{dl} is time-dependent and therefore constitutes an essential variable. The parameters apart from those given in Table III are: $k_{poison}=10$, pH=3. The solid, dotted and dashed-dotted lines denote the locations of saddle-node Hopf and saddle-loop infinite period bifurcations, respectively. Cutting the two-parameter plot along the ordinate at a sufficiently high value of R, one recovers one-dimensional bifurcation plots as given in Figs. 4(b) and 6(b): sustained oscillations set in at the Hopf bifurcation line. With increasing U the limit cycles increase in period remaining stable up to the location of the saddle-loop bifurcation where the current oscillations disappear. Beyond this point the system falls off to the low-current steady state as described before. From Fig. 9 it is important to note that for values of R smaller than $\approx45\ \Omega$ there are no dynamical instabilities.

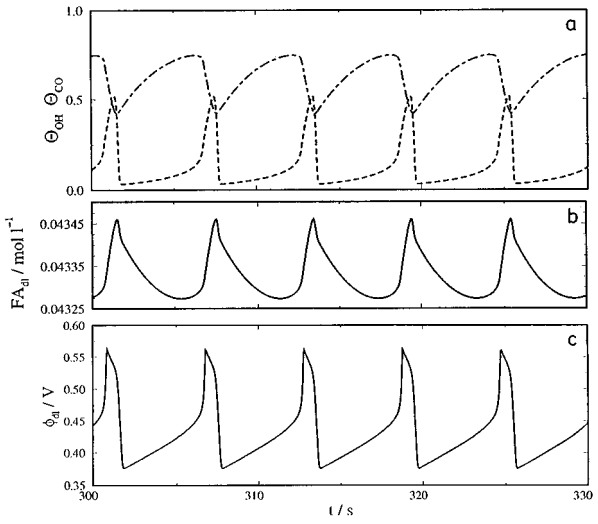

FIG. 8. Calculated time series of the four model variables at constant outer potential for parameters as in Fig. 6. (a) dashed line: θ_{OH}, dotted dashed line: θ_{CO}, (b) FA_{dl}, (c) ϕ_{dl}.

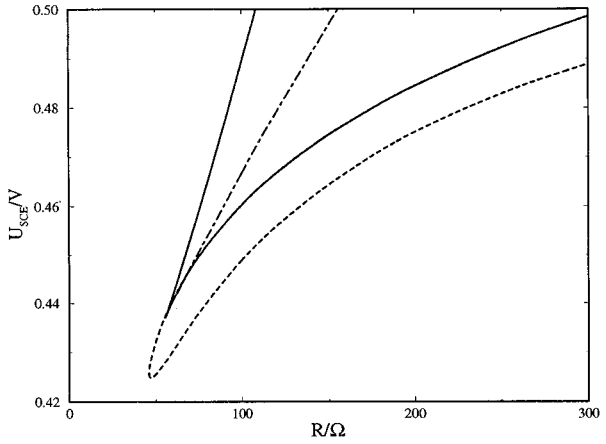

FIG. 9. Two-parameter bifurcation diagram of the complete FA model using $\delta=3\times10^{-2}$, $k_{poison}=10$ ℓ/mol s, pH=3. All other parameter as before. The solid line, dashed line and the dotted-dashed line indicate the location of the saddle-node bifurcations, the Hopf bifurcations and the saddle-loop bifurcations, respectively. All three curves meet in a Takens–Bogdanov point close to the cusp.

2. Suboscillator 1

In Section III we mentioned that small values of the diffusion layer thickness δ can be used to simulate strong stirring of the electrochemical bulk electrolyte.[19] Moreover, a small δ causes the diffusion fluxes to be large resulting in a rapid compensation of variations in concentrations of the variable FA_{dl}. Hence, one expects FA_{dl} to be nearly constant. In fact, experimentally, strong stirring is known to provide a quasi constant concentration of the electroactive bulk species. Simulating strong stirring (with $\delta=2\cdot10^{-4}$ cm) the concentration of FA_{dl} remained nearly constant at the bulk value of 0.05 mol/ℓ. As a species of constant concentration FA_{dl} does not constitute a model species essential for the observed dynamics.[21] The reduced network diagram showing the essential species and reactions as black arrows and symbols is shown in Fig. 10(a), whereas the nonessential species and (pseudo)reactions are shown in grey. The figure illustrates that under stirred conditions the observed dynamics is not based on the full model but instead stems from the dynamics of the black submechanism. The black subnetwork will henceforth be referred to as suboscillator 1.

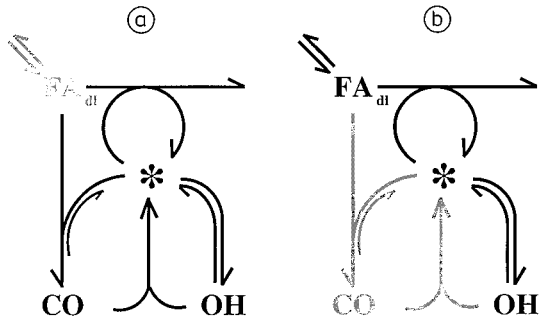

FIG. 10. (a) Network diagram of suboscillator 1. Only the black species and reactions are essential for the model dynamics. The grey species and reactions, i.e., the variable FA_{dl} as well as the diffusional transport reactions, have become nonessential by setting δ to a very small value thereby keeping FA_{dl} at its bulk concentration. (b) Network diagram of suboscillator 2. Similar to (a), only the black species and reactions are essential for the dynamics and are responsible for the observed dynamics. The rate of the poisoning reaction has been set to zero. Consequently, θ_{CO} as well as the rate of the removal reaction is zero.

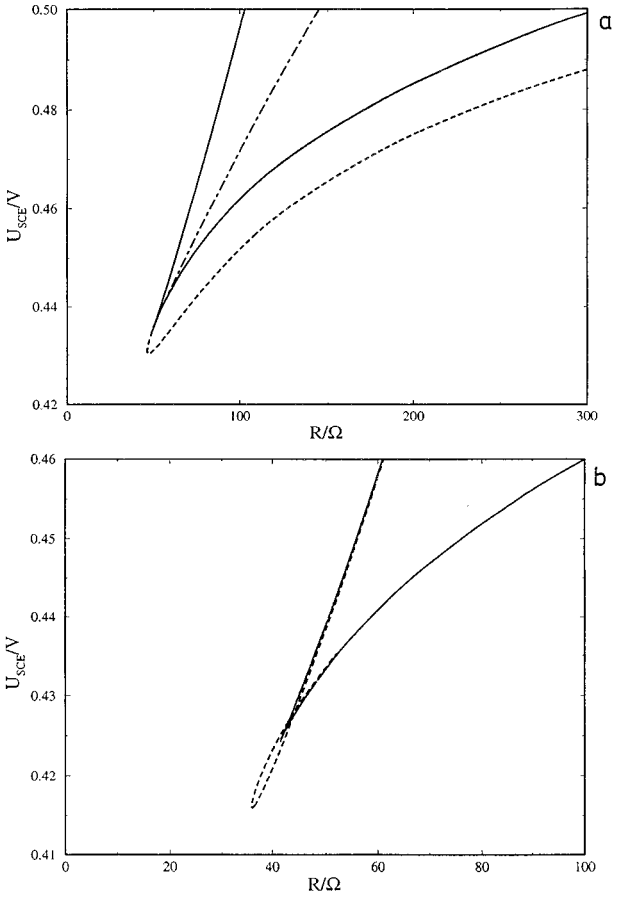

FIG. 11. (a) Two-parameter bifurcation diagram of suboscillator 1 using $\delta=2\times10^{-4}$, $k_{poison}=10$ ℓ/mol s, pH=3. All other parameters and linestyles as in Fig. 9. (b) Two-parameter bifurcation diagram of suboscillator 2 using $\delta=3\times10^{-2}$, $k_{poison}=10$ ℓ/mol s, pH=3. All other parameters and all linestyles as in Fig. 9.

A two-parameter bifurcation plot shown in Fig. 11(a) was calculated using the same set of model parameters as in the previous figure except for the values of δ. Although the cusp is slightly shifted towards smaller values of R and the potential region of stable limit cycles is slightly smaller, the diagram reveals a qualitatively very similar bifurcation structure as found for the full model. For a later discussion it is important to note that the Hopf bifurcation of suboscillator 1 is found on I/U curves with positive slope similar to the findings at large δ (unstirred conditions).

3. Suboscillator 2

We investigate the behavior of another submodel of the full FA mechanism. The simplified mechanism is obtained by setting the reaction rate of the poisoning reaction and consequently θ_{CO} constant to zero. This turns θ_{CO} into a

nonessential species as discussed in Ref. 21. The chemical part of the remaining submodel (from now on referred to as suboscillator 2) is shown by the black species and arrows in Fig. 10(b). As with suboscillator 1, the chemistry of suboscillator 2 is complemented by the equation for ϕ. Since we want FA_{dl} to be an essential model variable, we aim at a simulation of unstirred reaction conditions; this is achieved by simply setting δ back to $3 \cdot 10^{-2}$ cm. The two-parameter continuations of the local bifurcations are shown in Fig. 11b. The reduced set of chemical reactions is still able to exhibit limit cycle oscillations when interacting with the electrical variable ϕ. Although the location of the saddle-node bifurcations are similar as before, the oscillatory region is now very small compared to suboscillator 1 or to the unstirred full FA model. Again, the presence of a sufficiently large ohmic resistance R is necessary to induce instabilities. The bifurcation sets of Fig. 11(b) represent a cross-shaped phase diagram (XPD) which is frequently encountered in the bifurcation behavior of oscillatory chemical systems.[30] Setting $\delta = 2 \cdot 10^{-4}$ cm, the value of FA_{dl} can nearly be kept constant at the bulk concentration. The bifurcation diagram now shows the saddle-node curves as before, but no Hopf bifurcation is found. Obviously, sub-oscillator 2 is a minimal oscillator with FA_{dl} being an essential species. This result further indicates that the saddle-node bifurcations and consequently the bistability are solely due to the interaction of the fast potential-dependent ad/desorption of OH in the presence of an ohmic resistance R and a current providing process such as given by Eq. (12).

C. Mixed-mode oscillations

Having investigated the bifurcation behavior of the minimal suboscillators 1 and 2 we come back to the dynamics of the full FA model under unstirred conditions. One would expect that the dynamics of the full FA model under unstirred conditions should be affected by the individual behavior of both minimal oscillators. For values of U and R far from the cusp bifurcation, one would expect a dynamical behavior similar to that of suboscillator 1 as confirmed in Fig. 9. Near the cusp, however, where both oscillatory submodels exhibit sustained limit cycles, a more complex dynamical regime is to be expected. Two calculated times series for $R = 50\ \Omega$ and for two closely adjacent values of U are shown in Figs. 12(a) and 12(b). These current oscillations are characterized by the occurrence of a number of small-amplitude sinusoidal oscillations interspersed with a fast and large relaxational current spike. This phenomenon is known as mixed-mode oscillations and has frequently been observed in models and experiments of chemical and electrochemical oscillators.[7,25,31–34] A comparison of the wave forms of the two minimal oscillators and the mixed-mode oscillations for the given parameters indicates that the small-amplitude oscillations stem from suboscillator 2, whereas the large relaxational spikes are due to submodel 1. In between stable mixed-mode regimes as shown in Fig. 12(a), there are nonperiodic regimes as shown in Fig. 12(c).

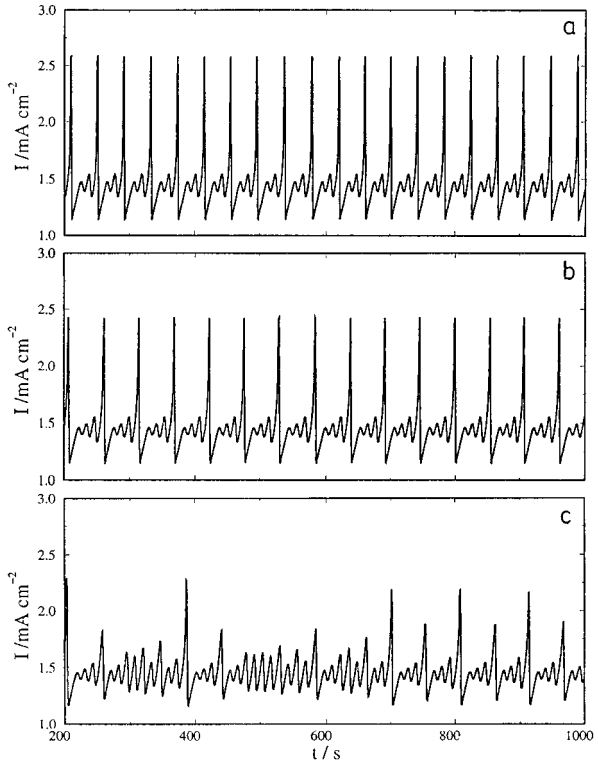

FIG. 12. Time series for $R = 50\ \Omega$ at different values of U. All other parameters as in Fig. 9. (a) mixed-mode oscillations (MMOs) characterized by one large-amplitude and two small-amplitude oscillations (1^2 state) at $U = 432.1$ mV, (b) mixed-mode oscillations characterized by one large-amplitude and three small-amplitude oscillations (1^3 state) at $U = 432.1155$ mV, (c) aperiodic oscillations at $U = 432.118$ mV.

VI. DISCUSSION AND COMPARISON TO EXPERIMENTS

A. CO oxidation

The model calculations on CO oxidation show that the assumption of a vacant site requirement in the kinetic rate law of reaction (4) is not needed; this assumption has frequently been made in previous FA studies[7,23,24,35,36] in order to account for the sharp rise in current density. Rather, the results in Section III suggest that the sharp current peak is due to a delayed OH adsorption which appears reasonable in view of a dense poisoning CO coverage. The vacant site mechanism would predict bistability under truly potentiostatic conditions in the presence of stirring, which was not observed.[1] Hysteresis, which may be interpreted as evidence for bistability, was only obtained in the absence of stirring. More recently, Okamoto *et al.*[14] suggested that OH (or H_2O) adsorption can only occur if CO is preadsorbed. We have found no evidence for such an assumption. In any case the model used (Sections II and III) was able to reproduce the experimental I/U curves using standard adsorption terms.

B. Formic acid oxidation

The model calculations revealed that the simple FA model is capable of reproducing the qualitative and many

semi-quantitative features of the experimental FA oxidation system. The value of the rate constant of the CO poisoning k_{poison} turned out to be a crucial parameter for the shape of the calculated cyclovoltammograms and the wave forms of the current oscillations. At high values of k_{poison}, both the scanned I/U curve and the stationary current oscillations resemble experimental findings on Pt(100) (see Fig. 9 in Ref. 1). This is seen by the occurrence of current spikes on both the anodic and cathodic potential scan and the rapid decrease in current during stationary oscillations. This result is consistent with chemical properties of Pt single crystal surfaces insofar as the rate of poisoning on Pt(100) is known to be larger than on the other two low-index single crystals.[27] The bifurcation behavior is again consistent with experimental findings:[1] at low potentials the stable steady state loses its stability via a supercritical Hopf bifurcation, whereas at high potentials U the oscillations disappear abruptly with finite amplitude in a saddle-loop bifurcation. At lower values of k_{poison}, the shape of the I/U curve changed in that no current spikes are seen on the cathodic scan, whereas large-period oscillations dominate the anodic scan. These results are consistent with experimentally measured cyclovoltammograms and oscillations on Pt(111) (see Fig. 11 in Ref. 1) where CO poisoning is known to proceed slowly. As for the phase relations of the chemical species, Fig. 8 confirmed the qualitative interpretations proposed in previous studies.[1] Furthermore, the numerically obtained bifurcation diagram in Fig. 9 is in agreement with the experimental bifurcation behavior (Fig. 14 in Ref. 1) with respect to the relative location of the different dynamical regimes.

C. Mechanistic analysis

In Section V, two oscillatory electrochemical subnetworks have been found to be present in the full FA model when δ was large (nonstirred conditions). Suboscillator 1, whose chemical part included the species and reactions shown in Fig. 10(a) as well as the double layer potential ϕ, was obtained when δ was chosen to be very small. In this case, the volume species FA_{dl} became nonessential for the dynamics and the remaining oscillatory subnetwork involved chemical surface species only. This means that suboscillator 1 is independent of stirring.

Suboscillator 2, in contrast, was found to consist of the chemical species and reactions shown in Fig. 10(b) (as well the electrochemical variable ϕ); the network involves the volume species FA_{dl} (which is sensitive to stirring), whereas θ_{CO} is nonessential. As for suboscillator 1, the fast reversible adsorption of OH remained essential for oscillations.

In general, oscillatory behavior requires the simultaneous presence of a fast positive as well as a slow negative feedback loop. For both oscillatory submechanisms 1 and 2, the fast positive feedback is given by the interplay of the free surface sites and the electrical variables ϕ and I as shown in Fig. 13(a). A solid (dashed) arrow indicates a positive (negative) influence. The arrows can also be pictured as representations of Jacobian elements between the variables shown. A feedback loop is given by the product of all Jacobian elements along the loop; thus, an even number of negative elements leads to positive, an odd number to negative feedback loops.

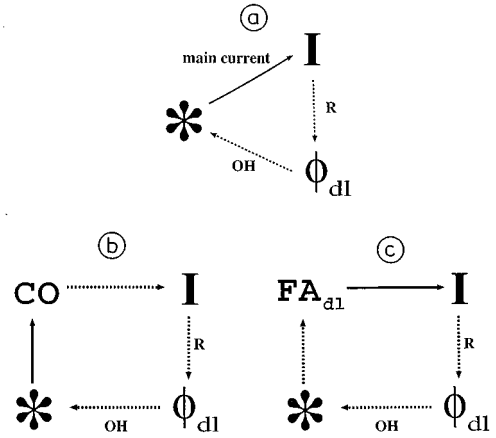

FIG. 13. (a) Positive feedback loop of both suboscillators. Solid arrows represent a positive, whereas dashed arrows indicate negative effect. The regulations can be viewed as matrix elements of a jacobian. Free surface sites affect the total current via the direct oxidation path. I effects ϕ_{dl} via the ohmic resistance and ϕ_{dl} feeds inversely back to the free surface sites due to the negative differential resistance. (b) Negative feedback loop of suboscillator 1. The loop contains the slow chemical species CO_{ad}. (c) Negative feedback loop of suboscillator 2. The loop includes the slow chemical species FA_{dl}.

The positive feedback loop in Fig. 13(a) operates as follows: Since the direct oxidation path [Eq. (12)] is the main current-carrying reaction, an increase of the number of free sites results in an increase in the total current I. An increasing current I, however, lowers ϕ which then leads to more free surface sites due to OH desorption. The potential dependent ad- and desorption of OH (in the presence of any current-carrying reaction) is seen to be crucial for a negative regulation between ϕ and I ($dI/d\phi<0$). This, however, is equivalent to saying that the ad- and desorption of OH constitutes the source of the negative differential resistance (NDR) which is known as crucial prerequisite for an electrochemical instability.

In the case of suboscillator 1, the negative feedback loop is depicted in Fig. 13(b). Again, the arrow style encodes the sign of the respective regulations. Now, a chemical species (CO) participates in the cycle whose rate of change occurs on a much slower time scale compared to the fast electrical variables ϕ and I. This slow chemical time scale determines the time scale of the entire loop leading to a slow negative feedback. Finally, the negative feedback loop of suboscillator 2 is shown in Fig. 13(c). Again, a slow chemical species (FA_{dl}) is rate determining for changes along the feedback cycle. It is clearly seen that if the variable FA_{dl} is nearly kept constant due to small values of δ, the negative feedback loop breaks down and oscillations disappear, whereas the positive feedback loop is still active and leads (in combination with the remaining chemical reactions) to bistability.

The oscillatory region in the parameter space of suboscillator 1 was seen to be very similar to that observed for large values of δ (nonstirred conditions). Obviously, the

dynamics of the unstirred FA system is mainly dominated by suboscillator 1. The oscillatory region of submodel 2, in contrast, was smaller overlapping with that of suboscillator 1 in a parameter region near the cusp. For parameters inside or close to this overlapping region, the dynamics of the nonstirred model (large δ) should be expected to be governed by both oscillators. In fact, the results of Section V C confirmed the presence of a parameter region of mixed-mode oscillations (MMOs). It should be noted that the MMO parameter region was small similar to what has been found in Ref. 32. As observed in other models of electrocatalytic systems,[25,32] there are also nonperiodic regimes adjacent to mixed-mode behavior.

The results given in the previous paragraph offer a consistent interpretation of the experimentally observed stirring effects described in Ref. 1: The experimental period-1 oscillations were generally found to be independent of stirring. This corresponds to the period-1 oscillations of suboscillator 1 which are independent of the diffusion layer thickness δ. Moreover, in experiments the MMOs were found to transform into period-1 oscillations as stirring was switched on. With stirred electrolyte MMOs have never been observed. This corresponds to the above results in that the mixed-mode behavior without stirring is due to the interplay of suboscillator 1 and 2; as stirring is switched on, the negative feedback of submodel 2 is suppressed, whereas suboscillator 1 survives.

D. Mechanistic classification

In Refs. 13 and 37, a classification of electrochemical oscillators was undertaken. Besides systems which are already oscillatory or bistable under strictly potentiostatic conditions (not relevant for the present discussion), two categories of electrochemical oscillators were described which require a negative differential resistance $dI/d\phi$ for an instability to occur. The first category includes systems that exhibit a negative slope in steady-state I/U characteristic. Current oscillations[10] are only observed on the branch of a negative slope. Under galvanostatic conditions, these systems show bistability only. Examples of oscillatory systems which fall into this category are the oxidation of peroxodisulphate or the reduction of metal cations in the presence of anionic catalysts.[8–11] The second category comprises systems that exhibit current oscillations on a branch of positive polarization slope. They exhibit potential oscillations under galvanostatic control, as well. In their steady-state characteristics the negative impedance of the fast process is hidden by a process on a slower time scale which shows a positive polarization slope. Therefore, these systems are said to have a ''hidden'' negative impedance. A typical example for this category was found to be the oxidation of H_2 in the presence of metal cations (Cu^{2+}, Bi^{3+}) and halogenide anions.[13]

According to this categorization, suboscillator 1 of the FA mechanism can be considered as a further example of a system with hidden negative impedance. Current oscillations occur on branches of positive polarization slope; under galvanostatic conditions, suboscillator 1 exhibits sustained potential oscillations. It is interesting to note the analogy between the mechanistic roles of the species in suboscillator 1 and the H_2 oxidation system. Similar to Cl^- during hydrogen oxidation, the fast ad/desorption of OH is responsible for the existence of a branch of negative impedance; the slower poisoning and reactive removal of CO in suboscillator 1 corresponds to the potential dependent ad/desorption of the metal cations, and the diffusion limited H_2 oxidation current and the direct oxidation path of FA constitute the current carrying processes of the respective oscillators. In suboscillator 2, the current carrying process as well as the process leading to a branch of negative impedance are the same as in suboscillator 1. The negative feedback species (volume species FA_{dl}), however, is now directly involved in the current carrying precess, similar to findings in the peroxodisulphate oscillator (first category). In the simulations, current oscillations occur on I/U branches of negative slope and at low stirring rates only, whereas under galvanostatic conditions, no potential oscillations are observable. Obviously, the FA oxidation model without stirring combines two oscillators, one from each category.

The observed phase diagrams of the two submodels are consistent with recent suggestions by Koper[37] as to the relation of oscillator category and bifurcation behavior. According to Ref. 37, oscillators of the first category (suboscillator 2) exhibit a cross-shaped phase diagram, whereas in the second category (suboscillator 1) ''the symmetry between the potential dependence of the charge balance of the electrified interface and the mass balance of the electroactive species'' is broken, and a different bifurcation scheme is obtained (Fig. 11).

The foregoing discussion strongly suggests a conclusion regarding the minimal mechanistic requirements for an electrocatalytic oscillator of the two categories considered here:[37] oscillators with hidden negative impedance require

(1) a current-carrying process (such as the direct FA oxidation or the H_2 oxidation for suboscillator 1 and the H_2 system, respectively) which may or may not depend on the potential,
(2) a process on a time scale comparable to that of variations of ϕ which is responsible for the occurrence of the negative differential resistance (fast potential-dependent ad/desorption of OH or halogenides) and
(3) a slower potential-dependent process exhibiting a positive current/potential characteristic (adsorption and reactive removal of CO or ad/desorption of metal).

Oscillators of the other category (*peroxodisulphate-type*), however, usually include

(1) only one potential-dependent process of positive polarization slope which involves a slow electroactive species as educt and simultaneously serves as the current-carrying reaction (direct FA oxidation and peroxodisulphate oxidation) as well as
(2) some mechanistic feature which causes a negative impedance (fast OH ad/desorption in the case of suboscil-

lator 2 or Frumkin correction term for the $S_2O_8^{2-}$ oxidation[13]).

These conclusions allow systematic predictions as to whether or not the mechanistic structure of an electrochemical system is in principle able to show oscillations for an appropriate choice of parameters.

VII. SUMMARY

We have formulated a realistic kinetic description of formic acid oxidation under potentiostatic control. Many experimental features such as cyclovoltammograms, wave forms of oscillations, bifurcation behavior, mixed-mode oscillations and stirring effects were reproduced in numerical simulations. A mechanistic analysis of the model revealed that the interplay of two suboscillators is responsible for the observed model dynamics. Finally, a classification of the suboscillators allowed the categorization of the FA system with respect to other electrochemical oscillators.

ACKNOWLEDGMENT

One of the authors (P.S). gratefully acknowledges support by the Studienstiftung des deutschen Volkes.

[1] P. Strasser, M. Lübke, F. Raspel, M. Eiswirth, and G. Ertl, J. Chem. Phys. **107**, 979 (1997), preceding paper.
[2] H. Degn, J. Chem. Soc. Faraday Trans. **64**, 1348 (1968).
[3] R. De Levie, Electroanal. Chem. Interfac. Electrochem. **25**, 257 (1970).
[4] T. Yamazaki, T. Kodera, R. Ohnishi, and M. Masuda, Electrochim. Acta. **35**, 431 (1990).
[5] T. Yamazaki and T. Kodera, Electrochim. Acta **36**, 639 (1991).
[6] T. Kodera, T. Yamazaki, M. Masuda, and R. Ohnishi, Electrochim. Acta **33**, 537 (1988).
[7] F. N. Albahadily and M. Schell, J. Electroanal. Chem. **308**, 151 (1991).
[8] M. T. M. Koper, P. Gaspard, and J. H. Sluyters, J. Phys. Chem. **96**, 5674 (1992).
[9] M. T. M. Koper and J. H. Sluyters, Electroanal. Chem. Interfac. Electrochem. **352**, 51 (1993).
[10] M. T. M. Koper and J. H. Sluyters, J. Electroanal. Chem. **371**, 149 (1994).
[11] W. Wolf, J. Ye, M. Purgand, M. Eiswirth, and K. Doblhofer, Ber. Bunsenges. Phys. Chem. **96**, 1797 (1992).
[12] F. Raspel and M. Eiswirth, J. Phys. Chem. **98**, 7613 (1994).
[13] W. Wolf, M. Lübke, M. T. M. Koper, K. Krischer, M. Eiswirth, and G. Ertl, J. Electroanal. Chem. **399**, 185 (1995).
[14] H. Okamoto, Chem. Phys. Lett. **248**, 289 (1996).
[15] R. Parsons and T. VanderNoot, J. Electroanal. Chem. **257**, 9 (1988).
[16] B. Beden, C. Lamy, N. R. D. Tacconi, and A. J. Arvia, Electrochim. Acta **35**, 691 (1990).
[17] B. Beden, J.M. Leger, and C. Lamy, in *Modern Aspects of Electrochemistry* (Plenum, New York, 1992), Vol. 22, p. 97.
[18] M. T. M. Koper and J. H. Sluyters, Electroanal. Chem. Interfac. Electrochem. **303**, 73 (1991).
[19] A. J. Bard and L. R. Faulkner, *Electrochemical Methods; Fundamentals and Applications* (Wiley, New York, 1980).
[20] B. L. Clarke, Adv. Chem. Phys. **42**, 1 (1980).
[21] M. Eiswirth, A. Freund, and J. Ross, Adv. Chem. Phys. **80**, 127 (1991).
[22] A.C. Hindmarsh, in *Scientific Computing*, edited by R. S. Stepleman (North-Holland, Amsterdam, 1983).
[23] N. Markovic and P. N. Ross, J. Phys. Chem. **97**, 9771 (1993).
[24] J. Wojtowicz, N. Marincic, and B. E. Conway. J. Chem. Phys. **48**, 4333 (1968).
[25] M. T. M. Koper and P. Gaspard, J. Phys. Chem. **95**, 4945 (1991).
[26] J. E. Doedel, *AUTO - Software for Continuation and Bifurcation Problems in Ordinary Differential Equations* (California Institute of Technology Press, Pasadena, CA, 1986).
[27] S. Motoo and N. Furuya, J. Electroanal. Chem. **184**, 303 (1985).
[28] A. Tripkovic, K. Popovic, and R. R. Adzic, J. Chim. Phys. **88**, 1635 (1991).
[29] F. Raspel, R. J. Nichols, and D. M. Kolb, J. Electroanal. Chem. **286**, 279 (1990).
[30] J. Boissonade and P. De Kepper, J. Phys. Chem. **84**, 501 (1980).
[31] I. Schreiber and M. Marek, Physica D **5**, 258 (1982).
[32] M. T. M. Koper and P. Gaspard, J. Chem. Phys. **96**, 7797 (1992).
[33] M. T. M. Koper, Adv. Chem. Phys. **92**, 161 (1996).
[34] M. Schell, F. N. Albahadily, J. Safar, and Y. Xu, J. Phys. Chem. **93**, 4806 (1989).
[35] X. Cai and M. Schell, Electrochim. Acta **37**, 673 (1992).
[36] Y. Xu and M. Schell, J. Phys. Chem. **94**, 7137 (1990).
[37] M. T. M. Koper, J. Electroanal. Chem. **409**, 175 (1996).